The Astrophysical Journal, 851:62 (12pp), 2017 December 10 https://doi.org/10.3847/1538-4357/aa988d

Correlated Signatures of Gravitational-wave and Neutrino Emission in Three-dimensional General-relativistic Core-collapse Supernova Simulations

Takami Kuroda[1], Kei Kotake[2,3], Kazuhiro Hayama[4], and Tomoya Takiwaki[5]
[1] Institut für Kernphysik, Technische Universität Darmstadt, Schlossgartenstrasse 9, D-64289 Darmstadt, Germany
[2] Department of Applied Physics, Fukuoka University, 8-19-1, Jonan, Nanakuma, Fukuoka, 814-0180, Japan
[3] Max Planck Institut für Astrophysik, Karl-Schwarzschild-Str. 1, D-85748, Garching, Germany
[4] KAGRA Observatory, Institute for Cosmic Ray Research, University of Tokyo, 238 Higashi Mozumi, Kamioka, Hida, Gifu 506-1205, Japan
[5] Division of Theoretical Astronomy, National Astronomical Observatory of Japan, 2-21-1, Osawa, Mitaka, Tokyo, 181-8588, Japan
Received 2017 August 4; revised 2017 October 24; accepted 2017 November 3; published 2017 December 12

Abstract

We present results from general-relativistic (GR) three-dimensional (3D) core-collapse simulations with approximate neutrino transport for three nonrotating progenitors (11.2, 15, and 40 $M_{\odot}$) using different nuclear equations of state (EOSs). We find that the combination of progenitor's higher compactness at bounce and the use of softer EOS leads to stronger activity of the standing accretion shock instability (SASI). We confirm previous predications that the SASI produces characteristic time modulations both in neutrino and gravitational-wave (GW) signals. By performing a correlation analysis of the SASI-modulated neutrino and GW signals, we find that the correlation becomes highest when we take into account the time-delay effect due to the advection of material from the neutrino sphere to the proto-neutron star core surface. Our results suggest that the correlation of the neutrino and GW signals, if detected, would provide a new signature of the vigorous SASI activity in the supernova core, which can be hardly seen if neutrino-convection dominates over the SASI.

Key words: gravitational waves – hydrodynamics – neutrinos – supernovae: general

1. Introduction

Core-collapse supernovae (CCSNe) have been attracting the attention of theoretical and observational astrophysicists for many decades. From multi-wavelength electromagnetic (EM) wave signals, a wide variety of observational evidence has been reported so far including ejecta/line morphologies, spatial distributions of heavy elements, and proper motions of pulsars, which have all pointed toward CCSNe being generally aspherical (e.g., Larsson et al. 2016; Grefenstette et al. 2017; Holland-Ashford et al. 2017; Tanaka et al. 2017 and references therein). As unambiguously important as these discoveries are, the EM signals could only provide an indirect probe of the explosion mechanism of CCSNe, because they take snapshot images of optically thin regions far away from the central engine.

Neutrinos and gravitational waves (GWs) are expected to provide direct probes of the inner-workings of CCSNe (e.g., Kotake 2013; Mirizzi et al. 2016 for a review). Currently, multiple neutrino detectors capable of detecting CCSN neutrinos are in operation (e.g., Scholberg 2012 for a review). The best suited detectors are *Super-Kamiokande* (Super-K) and IceCube, which can detect a rich data set of neutrino events (for example, $\sim 10^4$ for Super-K) from future Galactic CCSNe (Ikeda et al. 2007; Abbasi et al. 2011a). In the past 30 years after SN1987A—the only CCSN with neutrino detection to date (Bionta et al. 1987; Hirata et al. 1987), significant progress has also been made in GW detectors (e.g., Sathyaprakash & Schutz 2009 for a review). The sensitivity has been significantly enhanced enough to allow the first detection by the LIGO collaboration for the black hole merger event (Abbott et al. 2016). The second-generation detectors like advanced VIRGO (Hild et al. 2009) and KAGRA (Aso et al. 2013) will be online in the coming years. Furthermore, third-generation detectors like the Einstein Telescope and Cosmic Explorer have recently been proposed (Punturo et al. 2014; Abbott et al. 2017). At such a high level of sensitivity, CCSNe are also expected as some of the most promising astrophysical sources of GWs (e.g., Ott 2009; Fryer & New 2011; Kotake & Kuroda 2016 for review).

From a theoretical point of view, neutrino radiation-hydrodynamics simulations of CCSNe are converging to a point that multi-dimensional (multi-D) hydrodynamics instabilities, including neutrino-driven convection (e.g., Hanke et al. 2012; Couch 2013; Murphy et al. 2013) and the Standing-Accretion-Shock-Instability (SASI, Blondin et al. 2003; Foglizzo et al. 2006; Fernández 2015), play a crucial key role in facilitating the neutrino mechanism of CCSNe (Bethe 1990). In fact, a number of self-consistent models in two or three spatial dimensions (2D, 3D) now report revival of the stalled bounce shock into explosion by the "multi-D" neutrino mechanism (see Kotake et al. 2012; Burrows 2013; Foglizzo et al. 2015; Müller 2016; Janka 2017 for reviews).[6]

Conventionally, the GW and neutrino signatures from CCSNe have been studied rather separately. For the neutrino signals, Tamborra et al. (2013) were the first to find the SASI-induced modulations in the neutrino signals using results from full-scale 3D CCSN models (Hanke et al. 2013). They found that the SASI-induced modulation is clearly visible for two high-mass progenitors (20 and 27 $M_{\odot}$), where high SASI activity was observed in the post-bounce (pb) phase (Tamborra et al. 2014b). They pointed out that the frequency of the SASI-induced neutrino

[6] Here we shall consider canonical CCSN progenitors (Heger et al. 2005), where rotation/magnetic fields play only a small role in the explosion dynamics (see, however, Mösta et al. 2014; Takiwaki et al. 2016; Obergaulinger & Aloy 2017).

emission peaks around ∼80 Hz, which can be detectable by IceCube or the future *Hyper-Kamiokande* (Hyper-K) for a Galactic event at a distance of ∼10 kpc (see also Marek et al. 2009; Lund et al. 2010; Brandt et al. 2011; Müller & Janka 2014).

From recent self-consistent 3D models, it becomes clear that SASI also produces a characteristic signature in the GW emission (Kuroda et al. 2016a; Andresen et al. 2017). There are several GW emission processes in the post-bounce phase, including prompt convection, neutrino-driven convection, proto-neutron star (PNS) convection, the SASI, and *g*-mode oscillation of the PNS surface (e.g., Müller & Janka 1997; Müller et al. 2004, 2013; Kotake et al. 2009; Murphy et al. 2009; Cerdá-Durán et al. 2013). Among them, the most distinct GW emission process generically seen in recent self-consistent CCSN models is the one from the PNS surface oscillation (Müller et al. 2013; Kuroda et al. 2016a; Andresen et al. 2017; Yakunin et al. 2017). The characteristic GW frequency increases almost monotonically with time due to an accumulating accretion to the PNS, which ranges from ∼100 Hz to ∼1000 Hz in the typical simulation timescales. On the other hand, the GW frequency from the SASI appears in the lower-frequency range of ∼100 to 250 Hz and persists when SASI dominates over neutrino-driven convection (Kuroda et al. 2016a; Andresen et al. 2017). Andresen et al. (2017) pointed out that third-generation detectors (like ET) could distinguish SASI- from convection-dominated cases among their full-scale 3D models (Hanke et al. 2013; Melson et al. 2015) at a distance of ∼10 kpc.

These findings may raise a simple question of whether there is some correlation between the SASI-induced neutrino and GW signals. Spotted by the neutrino and GW astronomy in the advanced era, the time is ripe to study in detail what we can learn about the explosion mechanism from the future *simulatenous* detection of neutrinos and GWs using outcomes of multi-D CCSN models. In our previous work (Kuroda et al. 2016a), we have investigated the GW signatures based on 3D full-GR simulations with approximate neutrino transport for a nonrotating 15 $M_\odot$ star, using three different EOSs. In this work, we will compute two more progenitors of low- or high-progenitor compactness (11.2 and 40 $M_\odot$). Following Tamborra et al. (2014b), we estimate neutrino event rates in both Hyper-K and IceCube from our 3D-GR models. We perform a correlation analysis between the GW and neutrino signals. We discuss what we can learn about the supernova engine if the simultaneous detection is made possible for a next CCSN event.

This paper is organized as follows. We first give a short summary of the numerical setup and the extraction of GWs in Section 2. In Section 3, we present a short overview of hydrodynamics of our models. We then present analysis on the GW signatures in Section 4. The correlation analysis between the GW and neutrino signals is presented in Section 5. We summarize the results and discuss its implications in Section 6.

2. Numerical Methods and Initial Models

The numerical schemes for our 3D-GR models are essentially the same as those in Kuroda et al. (2016a). For the metric evolution, we employ the standard BSSN variables ($\tilde{\gamma}_{ij}$, ϕ, $\tilde{A}_{ij}$, K, and $\tilde{\Gamma}^i$; Shibata & Nakamura 1995; Baumgarte & Shapiro 1999). Solving the evolution equations of metric, hydrodynamics, and neutrino radiation in an operator-splitting manner, the system evolves self-consistently as a whole, satisfying the Hamiltonian and momentum constraints (Kuroda et al. 2012, 2014). The total stress-energy tensor is $T^{\alpha\beta}_{(\mathrm{total})} = T^{\alpha\beta}_{(\mathrm{fluid})} + \sum_\nu T^{\alpha\beta}_{(\nu)}$, where $T^{\alpha\beta}_{(\mathrm{fluid})}$ and $T^{\alpha\beta}_{(\nu)}$ are the stress-energy tensor of fluid and the neutrino radiation field, respectively. We consider three flavors of neutrinos ($\nu \in \nu_e, \bar{\nu}_e, \nu_x$) with ν_x representing heavy-lepton neutrinos (i.e., ν_μ, ν_τ and their anti-particles). All radiation and hydrodynamical variables are evolved in a conservative form. To follow the 3D hydrodynamics up to $\lesssim$200 ms post-bounce,[7] we shall omit the energy dependence of the radiation in this work (see, however, Kuroda et al. 2016b; Roberts et al. 2016).

We use three EOSs based on the relativistic-mean-field theory with different nuclear interaction treatments, which are DD2 and TM1 of Hempel & Schaffner-Bielich (2010) and SFHx of Steiner et al. (2013). For SFHx, DD2, and TM1,[8] the maximum gravitational mass (M_{max}) and the radius (R) of cold neutron star (NS) in the vertical part of the mass–radius relationship are $M_{\mathrm{max}} = 2.13$, 2.42, and 2.21 $M_\odot$ and $R \sim 12$, 13, and 14.5 km, respectively (Fischer et al. 2014). SFHx is thus softest followed in order by DD2 and TM1. Among the three EOSs, DD2 is constructed in a way that fits well with nuclear experiments (Lattimer & Lim 2013), whereas SFHx is the best-fit model with the observational mass–radius relationship (Steiner et al. 2013). All EOSs are compatible with the ∼2 $M_\odot$ NS mass measurement (Demorest et al. 2010; Antoniadis et al. 2013).

We study frequently used solar-metallicity models of a 15 $M_\odot$ star (Woosley & Weaver 1995), an 11.2 $M_\odot$ and a 40 $M_\odot$ star of Woosley et al. (2002), respectively. The 3D computational domain is a cubic box with 15,000 km width and nested boxes with eight refinement levels are embedded. Each box contains 128^3 cells and the minimum grid size near the origin is $\Delta x = 458$ m. In the vicinity of the stalled shock at a radius of ∼100 km, our resolution achieves $\Delta x \sim 1.9$ km, i.e., the effective angular resolution becomes ∼1°. Our 3D-GR models are named by the progenitor mass with the EOS in parenthesis like S15.0(SFHx), which represents the progenitor mass of 15.0 $M_\odot$ and the EOS SFHx are used.

We extract GWs from our simulations using the conventional quadrupole formula (Misner et al. 1973). The transverse and the trace-free gravitational field h_{ij} is

$$h_{ij}(\theta, \phi) = \frac{A_+(\theta, \phi)e_+ + A_\times(\theta, \phi)e_\times}{D}, \quad (1)$$

where $A_{+/\times}(\theta, \phi)$ represent amplitude of orthogonally polarized wave components with emission angle (θ, ϕ) dependence (Müller & Janka 1997; Scheidegger et al. 2010; Kuroda et al. 2014), $e_{+/\times}$ denote unit polarization tensors. In this work, we extract GWs along the north pole $(\theta, \phi) = (0, 0)$ and assume a source at a distance of $D = 10$ kpc.

[7] Note in Kuroda et al. (2016a) the data up to 350 ms post-bounce were shown. However, we are only able to compute up to ∼200 ms post-bounce for the newly added models (11.2 and 40 $M_\odot$) simply due to limited computational resources. To make the comparison fair (especially regarding the detectability; Figure 5), we shall often limit the analysis up to ∼200 ms post-bounce in this work (see, however, Figure 7).

[8] The symmetry energy S at nuclear saturation density is $S = 28.67$, 31.67, and 36.95 MeV, respectively (e.g., Fischer et al. 2014).

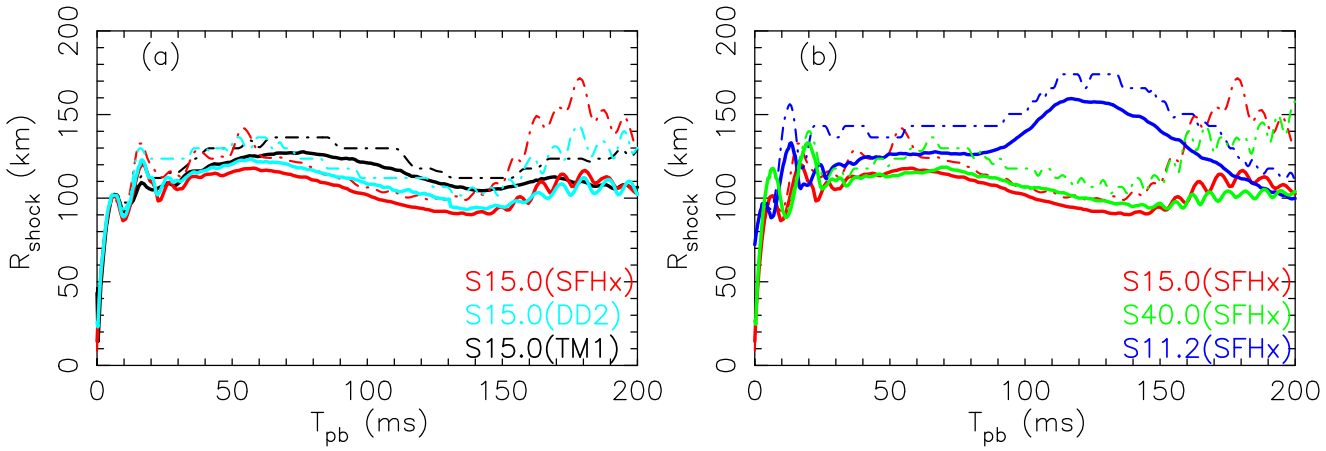

Figure 1. Time evolution of average (solid line) and maximum (dotted–dashed line) shock radii for all the models. The left and right panels compare the effect of EOSs and the progenitor masses, respectively.

Table 1
Progenitor's Compactness Parameter ($\xi_{1.5}$) and Key Quantities at Core Bounce (Labeled as "cb" in the Table) for All of the Computed Models

Model	$\xi_{1.5}$	$\rho_{c,cb}(10^{14}$ g cm$^{-3})$	$M_{cb}(M_\odot)$	$M_{cb}/R_{cb}(\%)$
S15.0(SFHx)	0.592	4.50	0.751	7.72
S15.0(DD2)	0.592	3.75	0.749	5.21
S15.0(TM1)	0.592	3.69	0.688	4.51
S11.2(SFHx)	0.195	4.23	0.663	4.84
S40.0(SFHx)	0.990	4.47	0.765	5.07

Note. Except for the compactness parameter (see the text for the definition), the maximum (rest-mass) density $\rho_{c,cb}$, the (unshocked) core mass M_{cb}, and its nondimensional relativistic parameter $M_{cb}/R_{cb}(=GM_{cb}/c^2R_{cb}$ in the cgs unit) are estimated at core bounce.

3. Overview of Hydrodynamics Features

In this section, we first present a short overview of hydrodynamics features in our 3D models for later convenience.

Table 1 compares progenitor's compactness parameter (O'Connor & Ott 2011; Nakamura et al. 2015) and several key quantities at core bounce for all the computed models in this work. For the compactness parameter, we adopt $M_{bary} = 1.5\,M_\odot$ at $t = 0$ of $\xi_{1.5} \equiv M_{bary}/M_\odot(R(M_{bary} = M)/1000\text{ km})^{-1}$ in the table. For the given progenitor mass (S15.0), one can see that the maximum density $\rho_{c,cb}$ becomes higher for the model with the softest EOS (SFHx). This is consistent with Fischer et al. (2014). Also the compactness parameter at bounce (M_{cb}/R_{cb}) has a correlation with the stiffness of the EOS. This is because the softer EOS leads to a more compact and massive unshocked core, which makes M_{cb}/R_{cb} higher. For the given EOS (SFHx), one can also see that the initial core compactness ($\xi_{1.5}$) has a non-monotonic impact on the compactness at bounce (compare M_{cb}/R_{cb} for S15.0(SFHx) and S40.0 (SFHx)). This is simply because the higher density profile in the precollapse phase leads to more massive inner-core (compare $\xi_{1.5}$ with M_{cb} in the table), which also makes the radius of the forming bounce shock bigger.

Figure 1 compares the evolution of the average (thick lines) and maximum (dashed–dotted lines) shock radii for models with different EOSs (panel (a)) and with different progenitor masses (panel (b)), respectively. Before $T_{pb} \sim 150$ ms (panel (a)), the average and maximum shock radii are smallest for SFHx (red thick line), followed in order by DD2 (turquoise line) and TM1 (black line), which is exactly the same as the stiffness of the EOS (SFHx:softest, TM1:stiffest). However, after the nonlinear phase sets in ($T_{pb} \gtrsim 150$ ms) when neutrino-driven convection and the SASI develop vigorously with time, the maximum shock radii of SFHx becomes biggest followed in order by DD2 and TM1. This reversal of the maximum shock radius before and after the nonlinear phase is due to the more stronger growth of the SASI for softer EOS. As previously identified (Scheck et al. 2008; Hanke et al. 2013), this is because the smaller shock radius and the more compact core (M_{cb}/R_{cb} in Table 1) lead to more efficient advective-acoustic cycle, i.e., the SASI activity (Foglizzo 2002; Foglizzo et al. 2006). Figure 2 visually supports this, where the large-scale shock deformation is most clearly seen for S15.0(SFHx) (top left panel), whereas the shock deformation is more modest for S15.0(DD2) (middle left panel) and for S15.0(TM1) (bottom left panel).

Panel (b) of Figure 1 compares the shock radii for the different progenitors with the same EOS (SFHx). S11.2(SFHx) shows the largest shock radii (average/maximum, blue lines) before $T_{pb} \lesssim 160$ ms. This is because prompt convection develops much more strongly for S11.2(SFHx). As consistent with Müller et al. (2013), this is because the prompt shock propagates rapidly due to the smaller mass accretion rate. Prompt convection is observed by formation of small-scale convective motions behind the roundish stalled shock (see the top right panel of Figure 2). The absence of clear SASI activity of this model is in accord with Hanke et al. (2013) and Müller (2016), where the 11.2 $M_\odot$ star was used in their self-consistent 3D models (but with different EOSs used). In panel (b), the average shock radius is slightly more compact for S15.0(SFHx) than S40.0(SFHx) in the linear phase ($T_{pb} \lesssim 150$ ms). In both S15.0(SFHx) and S40.0(SFHx), the SASI activity was similarly observed in the nonlinear phase (bottom panel of Figure 2), whereas the maximum shock radius is generally bigger for S15.0(SFHx). We ascribe this to the high SASI activity of S15.0(SFHx) compared to S40.0(SFHx) predominantly due to the more compact core (M_{cb}/R_{cb} in Table 1).

4. GW Signatures

In this section, we summarize how the hydrodynamics features in Section 3 impact the GW emission.

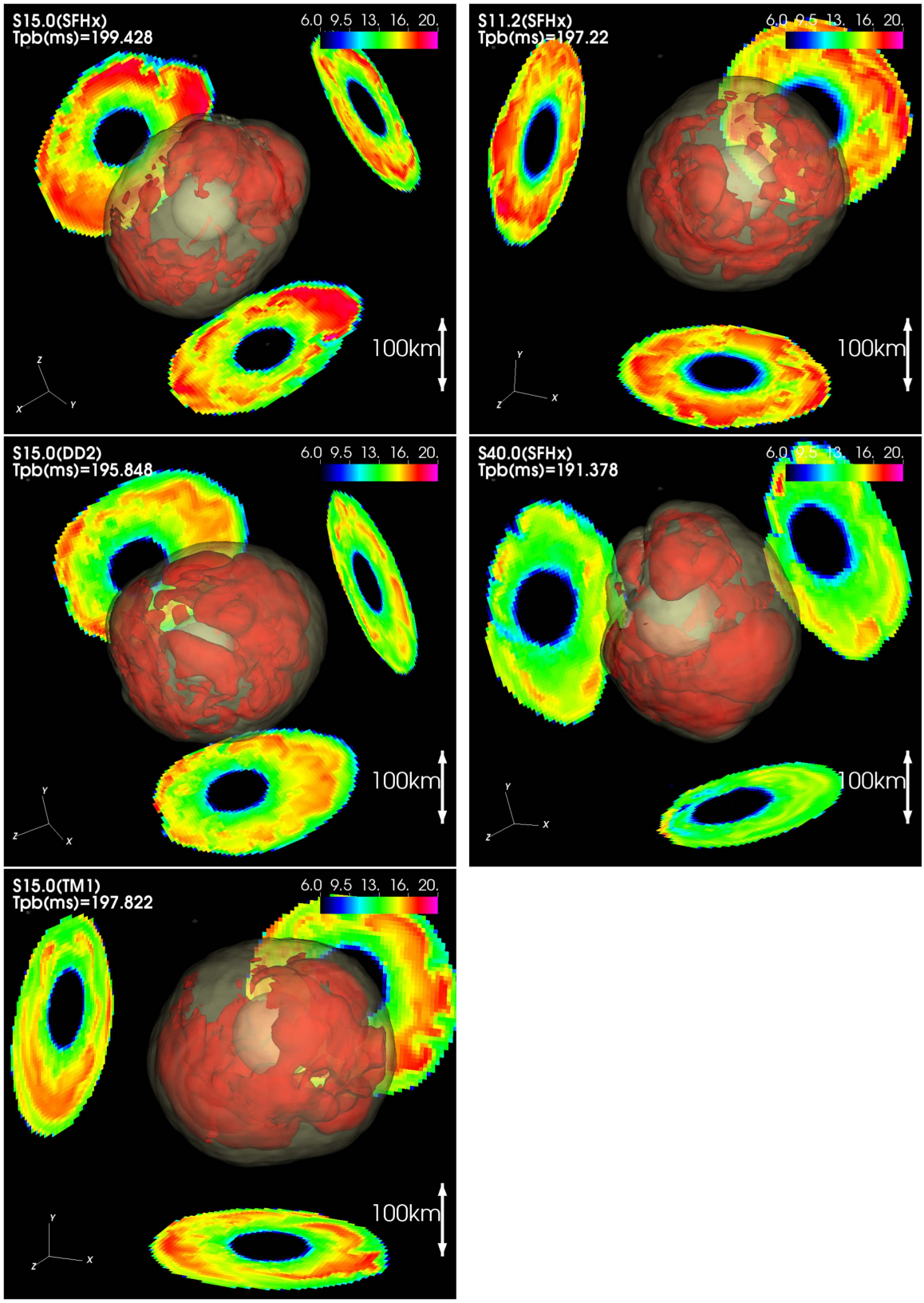

Figure 2. Snapshots showing hydrodynamics features of all the computed models at representative time snapshots. Shown are the isentropic surfaces for $s = 7\ k_{\rm B}$ baryon^{-1} (transparent shell) and for $s = 17\ k_{\rm B}$ baryon^{-1} (red bubbles; from top to bottom, left column; S15.0(SFHx), S15.0(DD2), and S15.0(TM1), right column; S11.2(SFHx) and S40.0(SFHx)). $T_{\rm pb}$ denotes the post-bounce time. The contours on the cross sections in the $x = 0$, $y = 0$, and $z = 0$ planes are projected on the sidewalls. The left column focuses on the EOS dependence. Top left and right columns show the progenitor mass dependence.

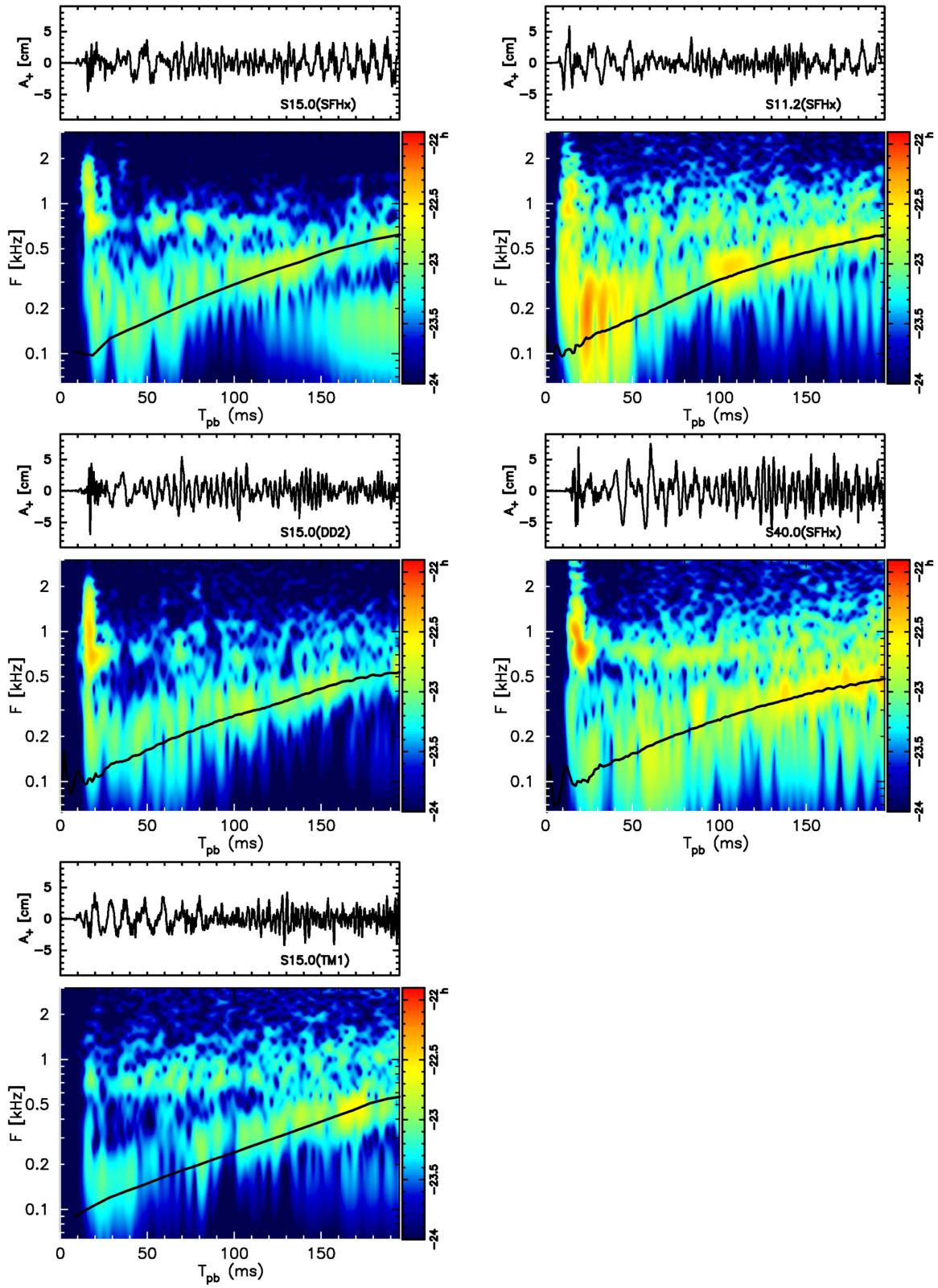

Figure 3. In each set of panels, we plot (top) the GW amplitude of plus mode A_+ [cm] and (bottom) the characteristic wave strain in the frequency-time domain $\tilde{h}$ in a logarithmic scale that is overplotted by the analytical GW frequency $F_{\rm peak}$ (black line) of the PNS g-mode oscillation (Marek & Janka 2009; Cerdá-Durán et al. 2013; Müller et al. 2013). We note that SFHx (top left) is the softest EOS followed in order by DD2 (middle left) and TM1 (bottom left), respectively. The top and middle right and panels are for S11.2(SFHx) and S40.0(SFHx), respectively.

Figure 3 shows time evolution of the GW amplitude (only plus mode A_+ and extracted along positive z-axis, black line) in the top panels and the characteristic wave strain in the frequency-time domain ($\tilde{h}(F)$, e.g., Equation (44) of Kuroda et al. 2014) in the bottom ones. Here F denotes the GW frequency. The top panels show a consistent GW behavior as

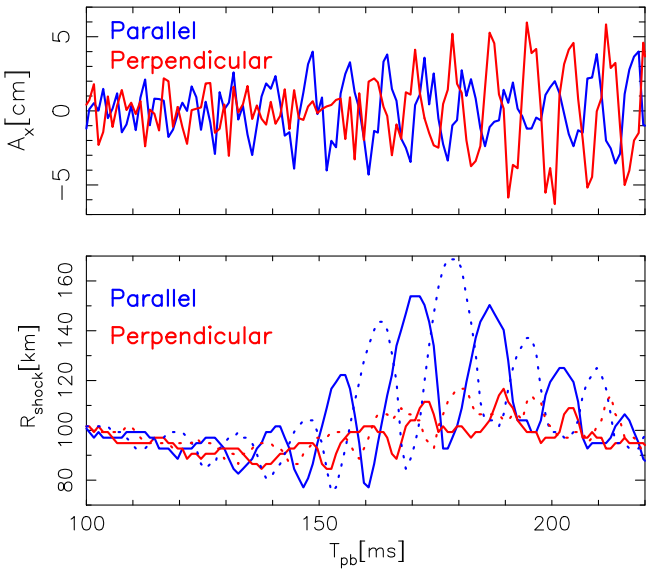

Figure 4. Time evolutions of the GW amplitudes (cross-mode, top) and shock positions (bottom). The color represents that the observer direction is parallel to the sloshing SASI axis (blue line) or perpendicular to the sloshing axis (red line, for a given azimuthal direction) in the top panel. In the bottom panel, the shock positions are measured along the two lines of sight with the same color in the top panel, where the solid and dotted curves correspond to the shock position at the nearest or farest to the observer along the line of sight, respectively.

previously identified in self-consistent models of Müller et al. (2013), Kuroda et al. (2016a), Andresen et al. (2017), and Yakunin et al. (2015). After bounce, the wave amplitude deviates from zero with low/high-frequency and relatively large spikes until $T_{pb} \sim 50$ ms. This is due to prompt convection. The GW from the prompt convection is shown to be biggest for S11.2(SFHx) (middle right panel). This comes from the vigorous prompt convection activity of this model as already mentioned in Section 3 (e.g., Figure 1(b)). It is consistent with Müller et al. (2013), who also showed a factor of ∼1.5 larger GW amplitude from prompt convection in the 11.2 $M_\odot$ model (G11.2) compared to that of $15M_\odot$ model (G15).

After prompt convection, no common features in the waveforms can be found among the models reflecting the stochastic nature of the post-bounce GWs. However, guided by the black line (Figure 3), one can see a relatively narrow-banded spectrum for all the models that shows an increasing trend in its peak frequency. In addition to this PNS g-mode contribution (Murphy et al. 2009; Cerdá-Durán et al. 2013; Müller et al. 2013), the SASI-induced low-frequency component is clearly seen for S15.0(SFHx) (e.g., the excess around $100 \lesssim F \lesssim 150$ Hz at $T_{pb} \gtrsim 150$ ms in the spectrogram; top left panel). Note that this is also observed in Andresen et al. (2017).

So far, we show results only for one representative observer direction (along positive z-axis), which is not a special direction relative to the SASI motion. Tamborra et al. (2014b) showed that the time modulation in neutrino signal has a dependence on the observer angle relative to the (sloshing) SASI motion. According to their results, the neutrino detection rate is significantly larger and also the time modulation is more clearly seen when the observer is along the axis of sloshing motion.

As we have discussed in Section 3 (see also Kuroda et al. 2016a), some of our models show vigorous sloshing SASI motion. To see the observer angle dependence on the GW, we plot the GW amplitudes (only for the cross-mode, top) and shock positions (bottom) as a function of post-bounce time in Figure 4 for model S15.0(SFHx). To plot this figure, we first determine two lines of sight. One is parallel to the sloshing axis and the other is an arbitrary direction but perpendicular to the sloshing axis. Then the color in Figure 4 represents that the observer direction is parallel (blue) or perpendicular (red) to the sloshing axis in the top panel. In the bottom panel, the shock positions are measured along these two lines of sight with the same color notation in the top panel. Two shock positions along each line of sight, near and far side to the observer, are plotted by different line styles, solid (near) and dotted (far), respectively. As a reference, the observer directions are $(\theta, \phi) \sim (135°, 0°)$ and $\sim(45°, 0°)$ for the parallel and perpendicular directions, respectively, at $T_{pb} \sim 180$ ms for S15.0(SFHx).

As one can see from the bottom panel, the shock position oscillates largely along the sloshing axis (blue lines) with nearly the opposite phase between the solid and dotted lines. On the other hand, the red lines show significantly smaller deviations. After the sloshing motion reaches its maxima at $T_{pb} \sim 180$ ms, the GW emitted toward the perpendicular direction reaches ∼5–6 cm at $180 \lesssim T_{pb} \lesssim 200$ ms. In the meantime, the GW amplitude reaches merely ∼2 cm along the parallel direction. Thus, contrary to the neutrino emission, the GW emission is stronger toward the orthogonal direction to the sloshing motion. This is analogous to the stronger GW emission toward the equatorial plane in the rotating progenitor model at bounce.

Regarding the EOS dependence, the GW spectrum extends to higher frequency for our model with the stiffest EOS (S15.0 (TM1), the black line in the left panel of Figure 5), whereas the GW spectrum for the softest EOS (S15.0(SFHx), red line) concentrates more in the lower-frequency domain. Note that an excess around $100 \lesssim F \lesssim 200$ Hz in the spectrum of S15.0 (SFHx) corresponds to the SASI-induced GW emission mentioned above.

As for the progenitor dependence, S40.0(SFHx) shows stronger GW emission compared to S11.2/15.0(SFHx) (e.g., bottom panel of Figure 3). In fact, the right panel of Figure 5 (green line) shows that the GW spectrum dominates over that of the other models over the wide frequency range. For this model, the signal-to-noise ratio reaches ∼10 around the best sensitivity around $F \sim 100$ Hz and a Galactic event could be likely to be detectable. But, in order to discuss the detectability of the signals more quantitatively, one needs a dedicated analysis (e.g., Hayama et al. 2015; Gossan et al. 2016; Powell et al. 2016), which is beyond the scope of this work.

5. Correlation between GW and Neutrino Emission

In this section, we present a correlation analysis between the GW (Section 4) and the neutrino signals.

For all the computed (five) models, we plot in Figure 6 the expected neutrino event rate (N_ν [ms^{-1}], red line) for Hyper-K (fiducial mass 440 kton, Abe 2016) and the GW amplitude A_+ (black line) in the top panel. In the bottom panel, the contours (red curves) correspond to the Fourier-decomposed anti-electron type neutrino event rates (two arbitrary chosen values of $dN_\nu/dF = 0.4$ (thin red line) and 0.8 (thick red line), only for $T_{pb} \geqslant 100$ ms) that is superimposed on the GW

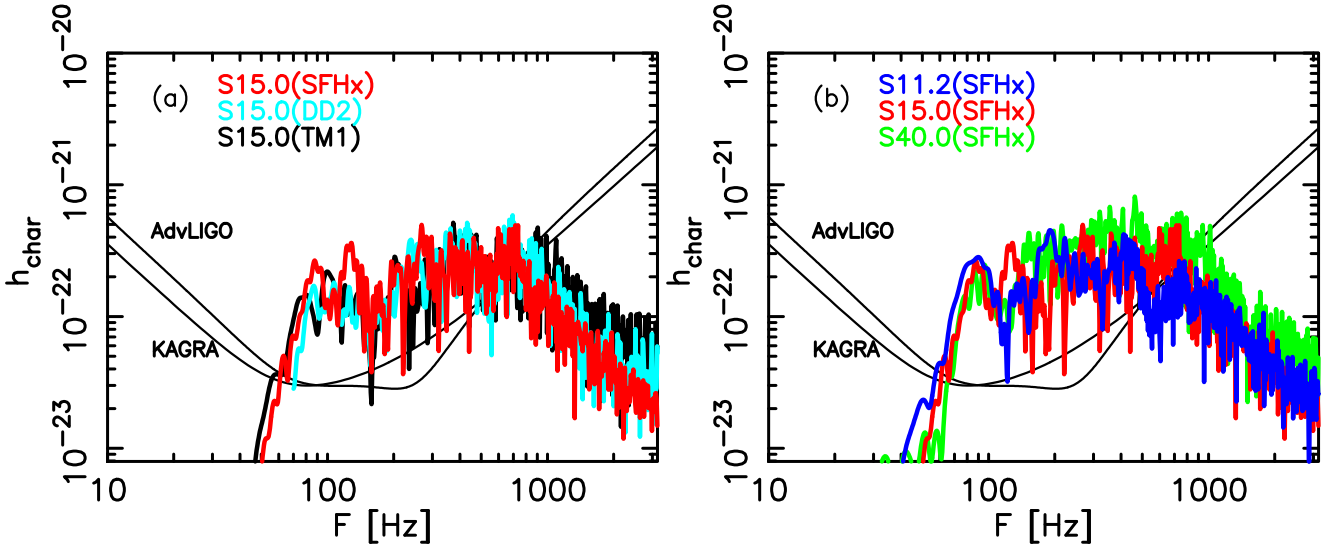

Figure 5. Same as Figure 1, but for the characteristic GW strain spectra for a source of distance at 10 kpc. We estimate the spectra for the time integration of the GW energy in the range of $0 \leqslant T_{\rm pb} \leqslant 200$ ms. Solid thin black curves denote the sensitivity curves of LIGO (Harry & LIGO Scientific Collaboration 2010) and KAGRA (Aso et al. 2013).

spectrograms. Similar to Figure 3, the observer direction for both neutrinos and GWs is fixed along the z-axis with a source distance of $D = 10$ kpc. Following the methods in Appendices A and B of Tamborra et al. (2014a), we estimate the expected neutrino event rate from our 3D models, where the flux-projection effects are also taken into account. Because the consideration of collective neutrino oscillation is beyond the scope of this work (e.g., Duan et al. 2010; Chakraborty et al. 2016; Mirizzi et al. 2016 for reviews), we show two extreme cases where the detector measures the original $\bar{\nu}_e$ (red line) or ν_x (green line) flux. The latter case corresponds to the complete flavor conversion through the Mikheyev–Smirnov–Wolfenstein (MSW) effect (Wolfenstein 1978; Mikheyev & Smirnov 1985).

Among the models in Figure 6, the top left panel (S15.0 (SFHx)) shows the clearest overlap between the neutrino modulation (see red contours in the spectrogram) and the GW modulation at $T_{\rm pb} \gtrsim 150$ ms in the frequency range of $F \sim 100$–150 Hz. For S15.0(TM1) with the stiffest EOS (middle left panel), the overlap between the quasi-periodic neutrino and GW signals can be marginally seen only at the higher frequency range $F \sim 400$–500 Hz after $T_{\rm pb} \sim 150$ ms, which is significantly weaker compared to S15.0(SFHx). Comparing S15.0(TM1) with S15.0(DD2) (top right panel), one can see a clearer quasi-periodic oscillation in the neutrino event rate for softer EOS (top right panel), although there is little correlation between the GW and neutrino signal in the spectrogram. In the smallest mass progenitor of S11.2(SFHx), we do not find any remarkable simultaneous oscillation of the neutrino and GW signals. For this model, the neutrino event rate becomes smallest among the five models and shows little time modulation (after $T_{\rm pb} \sim 100$ ms), which is consistent with Tamborra et al. (2014b). On the other hand, the most massive progenitor of S40.0(SFHx) has a largest overlap in the spectrogram (red contours) over the wide frequency range $50 \lesssim F \lesssim 500$ Hz.

When the complete flavor conversion between $\bar{\nu}_e$ and ν_x is assumed (green line at $T_{\rm pb} \gtrsim 150$ ms of model S15.0(SFHx) in Figure 6), the time modulation is significantly suppressed as already reported in Tamborra et al. (2013). This is because that the neutrino spheres of heavy-lepton neutrinos are located much deeper inside compared to those of anti-electron neutrinos. Consequently, they are less affected by the SASI activity and the correlation between the GW and the neutrino event rate becomes weaker in the case of the complete flavor swap.

We plot in Figure 7 power spectra of the neutrino events in IceCube (Abbasi et al. 2011b) to see impacts of the EOS and the progenitor. A pronounced peak is seen around ∼120 Hz in S15.0(SFHx) (red line), which is absent for other S15.0 models with weak SASI activity (green and blue lines). This is again consistent with Tamborra et al. (2013, 2014b). The absence of the SASI signature of the $11.2\,M_\odot$ model is in line with Tamborra et al. (2013). S40.0(SFHx) that has a relatively high compactness parameter (Table 1) exhibits SASI activity and shows a peak at $F \sim 160$ Hz. In addition to the biggest peak, some secondary peaks are also seen on the black line as well as in other models, e.g., at $F \sim 60$ Hz on the red line. In Tamborra et al. (2013), these secondary peaks are hard to see in most of the employed progenitors except for the $20\,M_\odot$ model. We consider that this difference might be partially due to our simplified transport scheme, where the neutrino matter coupling is controlled via several parameters (see Kuroda et al. (2012) for more details). Because of this, our neutrino signals may change more sensitively in response to the matter motion compared to those obtained in CCSN models with more sophisticated neutrino transport. For example, during the prompt convection phase ($T_{\rm pb} \lesssim 50$ ms), our neutrino event rate shows an oscillatory behavior (see red/green line in every top panel in Figure 6), which is not seen in Tamborra et al. (2013). To clarify this, we need to perform 3D-GR simulations with a more elaborate neutrino transport scheme, which is, unfortunately, computationally unaffordable at this stage.

From Figures 6 and 7, it has been shown that the SASI modulation frequency of both the GW and neutrino signals is relatively close (i.e., in the range of $100 \sim 200$ Hz). Figure 8 illustrates how the two signals could be spatially correlated. In the figure, the SASI flows (red dashed arrows) advecting from the shock first excite oscillation in the neutrino signal at the

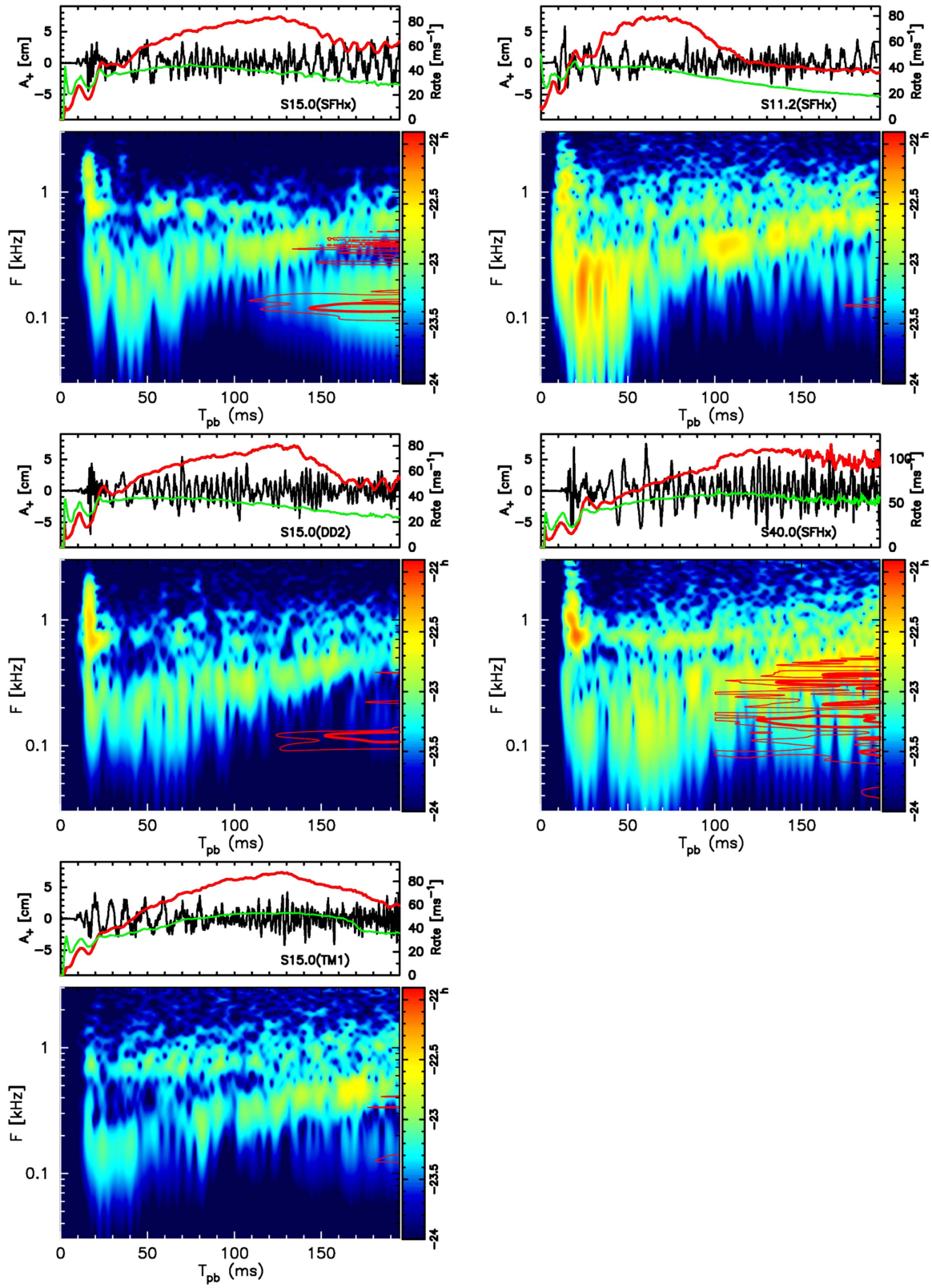

Figure 6. For each model, the top panel shows the neutrino event rate N_ν [ms^{-1}] (red and green lines are for $\bar{\nu}_e$ and ν_x, respectively) for Hyper-K and the GW amplitude A_+ [cm] (black line), whereas in the bottom panel we plot contours (red curves, only for $T_{\rm pb} \geqslant 100$ ms) of the anti-electron type neutrino spectra that are superimposed on the color-coded GW spectrum. The observer's direction is fixed along the z-axis for a source at a distance of $D = 10$ kpc.

(average) neutrino sphere. Afterward, it reaches to the PNS core surface (the blue thick arrows), leading to the modulation in the GW signal (see also Kuroda et al. 2016a for the detailed analysis). We can roughly estimate the time delay ΔT as follows. The radius of the anti-electron-type neutrino sphere is $R_{\bar{\nu}_e} \sim 37$ km and the PNS core surface is $R_{\rm PNS} \sim 15$ km (at

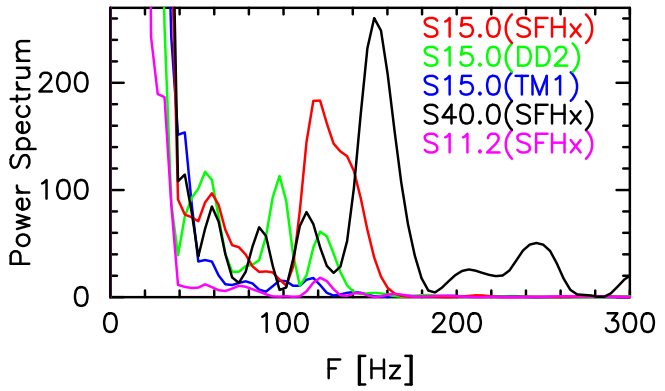

Figure 7. Power spectrum of the IceCube event rate for the time interval of $100 \leqslant T_{\rm pb} \leqslant 200$ ms.

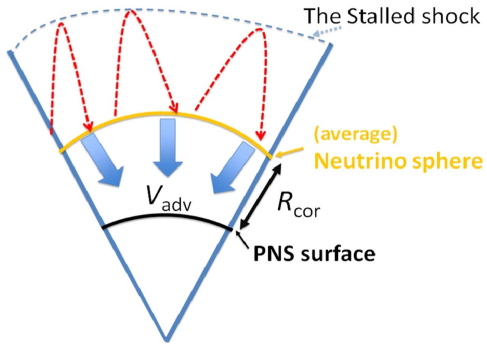

Figure 8. Schematic drawing to illustrate the different radial positions of SASI-induced neutrino and GW emission in the post-bounce core. Below the stalled shock (dashed blue line, labeled as "The stalled shock"), nonspherical flows (dashed red line with arrow) hit first the (average) neutrino sphere then penetrates into the PNS core surface. $R_{\rm cor}$ represents the distance between the neutrino sphere ($\bar{\nu}_e$ in this case) and the PNS. $V_{\rm adv}$ is the typical velocity of the downflows there.

$T_{\rm pb} = 200$ ms for S15.0(SFHx)), then the correlation distance is $R_{\rm cor} = R_{\bar{\nu}_e} - R_{\rm PNS} \sim 20$ km. An angle-average accretion velocity at $R = 40(20)$ km is $V_{\rm adv} \sim -1 \times 10^8 (-1 \times 10^7)$ cm s^{-1} at $T_{\rm pb} = 200$ ms, leading to ΔT of a few 10 ms.

In order to estimate the correlation between the neutrino and GW signal more quantitatively, we evaluate the correlation function $X(t, \Delta T)$ in Figures 9 and 10. Note that Figures 9 and 10 are for S15.0(SFHx) and S11.2(SFHx) showing highest and invisible SASI activity in this work, respectively.

The top panel of Figure 9 shows the GW amplitude (blue line) and the neutrino event rate (black and red lines) in arbitrary units. In order to focus on the SASI-induced modulation, the red curve is the event rate after the monotonicaly time-changing component is subtracted from the original curve (black line).[9]

We then evaluate the correlation between the GW (blue line) and neutrino (red line) signals by calculating the following normalized correlation function $X(t, \Delta T)$

$$X(t, \Delta T) = \frac{\int d\tau H(t-\tau) A_\nu(\tau + \Delta T) A_{\rm GW}(\tau)}{\sqrt{\int d\tau H(t-\tau)(A_\nu(\tau+\Delta T))^2}\sqrt{\int d\tau H(t-\tau)(A_{\rm GW}(\tau))^2}}, \quad (2)$$

where t is the post-bounce time and $H(t-\tau)$ is the Hann window with the window size of $|t-\tau| \leqslant 10$ ms. $A_\nu(t)$ and $A_{\rm GW}(t)$ is the neutrino event rate without the DC component and the GW amplitude, respectively. ΔT [ms] represents the time delay between the neutrino and GW signals and we take $0 \leqslant \Delta T \leqslant 24$ ms with a time interval of 4 ms. In the middle panel, we plot $X(t, \Delta T)$ for all ΔT in different colors as shown in the upper part of the panel. The bottom panel shows $\Delta T_{\rm max}$, which gives the maximum $X(t, \Delta T)$.

From the middle panels of Figure 9, we find a clear increment in $|X(t, \Delta T)|$ at $T_{\rm pb} \sim 150$ ms for both GW polarized modes. At this point in time, the SASI activity becomes strongest (see Figure 3 in Kuroda et al. 2016a). If we look at panel ($b+$), $|X(t, \Delta T)|$ with larger ΔT increases faster. $X(t, \Delta T = 24$ ms) increases fast with a positive value and then $X(t, \Delta T = 20$ ms) comes next, but with a negative value. Afterward, $X(t, \Delta T = 16$ ms), $X(t, \Delta T = 12$ ms), $\cdots$, follow with the same manner. Completely, an opposite trend can be seen in the $\times$ mode of the polarization (panel ($b\times$)), i.e., $X(t, \Delta T = 24$ ms), $X(t, \Delta T = 16$ ms), $\cdots$, show negative values and $X(t, \Delta T = 20$ ms), $X(t, \Delta T = 12$ ms), $\cdots$, show positive values. This can be explained by the correlation frequency $F \sim 120$ Hz (see the top left panel in Figure 6 and the left one in Figure 7). The corresponding time period $\sim$8 ms of $F \sim 120$ Hz leads to a cycle of negative and positive correlations if we shift neutrino count event with half of its value, i.e., $\sim$4 ms. Furthermore, the opposite trend between ($b+$) and ($b\times$) can be understood by the phase shift with a half period between the plus and cross-mode of GWs, since the leading term of the PNS deformation is the quadrupole ($l = 2$) mode (Kuroda et al. 2016a). From panels (c+/$\times$), $\Delta T_{\rm max}$ with $\sim$18 ms appears first in both polarization modes. It means that there is a time delay of GWs from neutrinos as $\Delta T \sim 18$ ms. Remarkably, this value is consistent with our previous rough measurement for the accretion timescale of a few 10 ms. Note that we have also done the same analysis for the rest of our models and found no significant correlation. As a reference, Figure 10 is shown for S11.2(SFHx), where there is no significant correlation between the GW and neutrino signals for this convection-dominated model.

6. Summary and Discussion

We have presented results from our 3D-GR core-collapse simulations with approximate neutrino transport for three nonrotating progenitors (11.2, 15, and 40 $M_\odot$) using three different EOSs. Among the five computed models, the SASI activity was only unseen for an 11.2 $M_\odot$ star. We have found that the combination of progenitor's higher compactness at bounce and the use of softer EOS leads to the stronger SASI activity. Our 3D-GR models have confirmed previous predications that the SASI produces characteristic time modulations both in the neutrino and GW signals. Among the computed models, a 15.0 $M_\odot$ model using SFHx EOS exhibited the most

[9] As one can see from the red line in each top panel in Figure 6, the neutrino event rate for $0 \lesssim T_{\rm pb} \lesssim 150$ ms is approximately fitted by a linear function (as a function of post-bounce time) with positive slope, whereas it can be fitted by a linear function with a negative slope plus the SASI modulation thereafter. When we evaluate the correlation function $X(t, \Delta T)$ in Equation (2), the large offset can be a hinderance for an appropriate evaluation of $X(t, \Delta T)$. We thus roughly remove the quasi-monotonically changing component, i.e., the offset, in a simple way as $A_\nu(t) \rightarrow A_\nu(t) - (A_\nu(t + \tau/2) + A_\nu(t - \tau/2))/2$. Here τ is a time window and we usually use $\tau = 60$ ms.

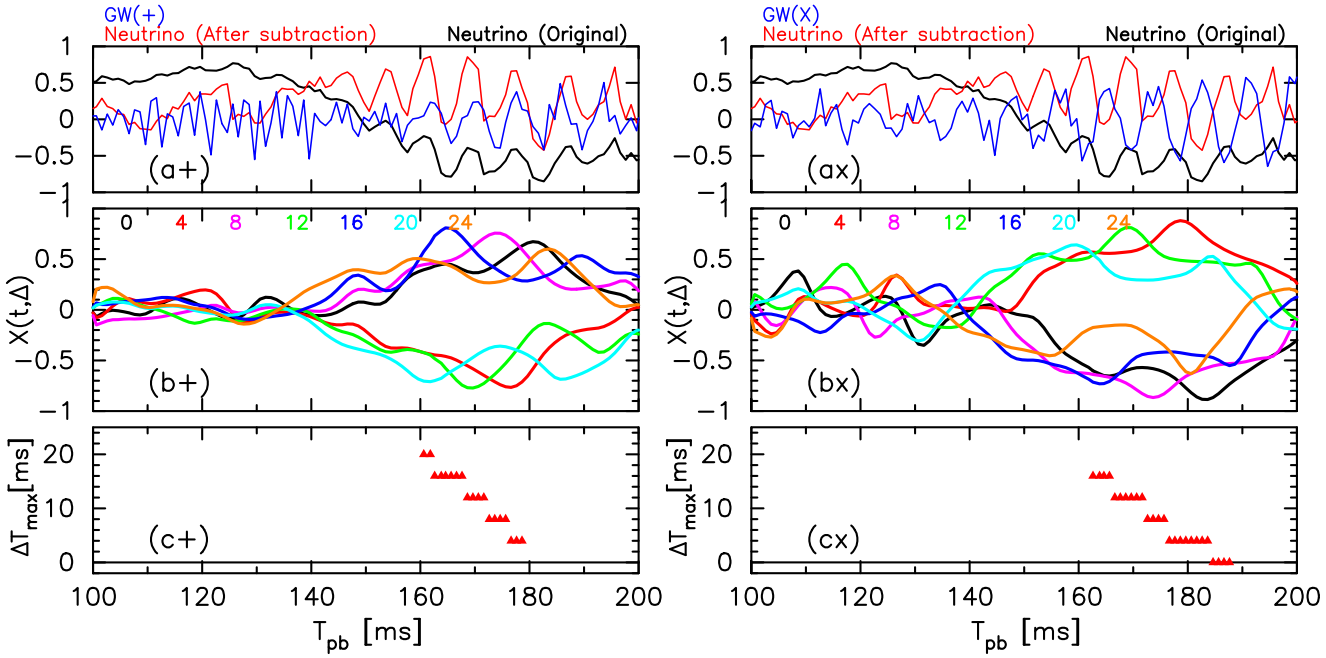

Figure 9. Top panels show the GW amplitude (blue line) either + (left panel) or × polarization (right panel) and the neutrino event rate (black and red lines) in arbitrary units for S15.0(SFHx). For the red line, the monotonically time-changing component of the black line is subtracted ($T_{\rm pb} \lesssim 170$ ms) in order to focus on the SASI-induced modulation. Same as the top panels, the middle panels ($b+/\times$) show the correlation function $X(t, \Delta T)$ between the GW amplitude (blue line, top) and the event rate (red line, top) with several time delay ΔT (see the text for the definition) which is indicated in the upper left part as 0, 4, 8, 12, 16, 20, and 24 [ms]. Bottom panels ($c+/\times$) show $\Delta T_{\rm max}$ that gives the delay time with the maximum correlation in the middle panels. Note when we obtain $\Delta T_{\rm max}$, we set an arbitral threshold as $|X(t, \Delta T)| \geqslant 0.7$ not to extract insignificant values.

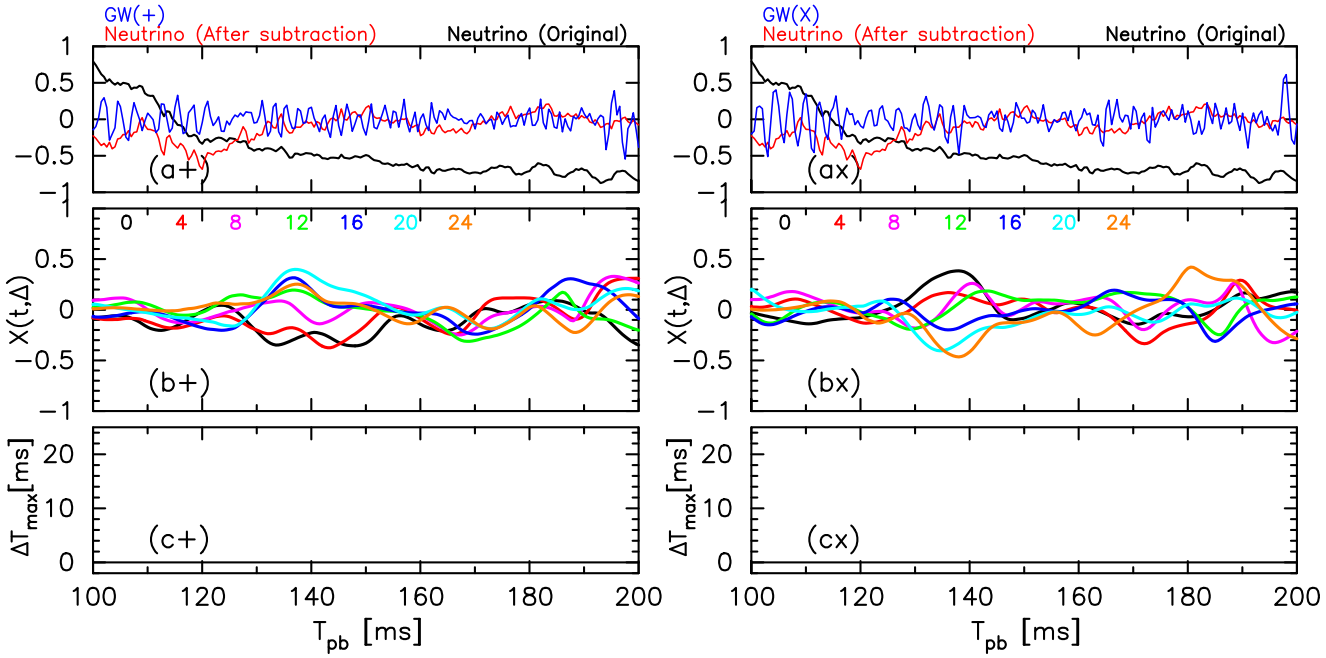

Figure 10. Same as Figure 9 but for S11.2(SFHx).

violent SASI motion, where the SASI-induced modulation in both GWs and neutrinos were most clearly observed. The typical modulation frequency is in the range of ∼100–200 Hz, which is consistent with the oscillation period of the SASI motion. By performing a correlation analysis between the SASI-induced neutrino and GW signatures, we have found that the correlation becomes highest when we take into account the time-delay effect due to the advection of material from the neutrino sphere to the PNS core surface. Our results suggest that the correlation of the neutrino and GW signals, if detected, could provide a new signature of the vigorous SASI activity in the supernova core, which can be barely seen (like for the $11.2\,M_{\odot}$ model) if neutrino-convection dominates over the SASI.

In order to enhance the predicative power of the neutrino and GW signals in this work, we need to at least update our M1 scheme from gray to multi-energy transport as in Kuroda et al. (2016b) and Roberts et al. (2016). Inclusion of detailed

neutrino opacities is also mendatory (e.g., Buras et al. 2006; Lentz et al. 2012; Martínez-Pinedo et al. 2012; Burrows et al. 2016; Fischer 2016; Bollig et al. 2017; Horowitz et al. 2017; Roberts & Reddy 2017). Impacts of rotation and magnetic fields (Mösta et al. 2014; Takiwaki et al. 2016; Obergaulinger & Aloy 2017) on the correlation between the GW and neutrino signals (Ott et al. 2012; Yokozawa et al. 2015) should be also revisited with 3D-GR models including more sophisticated neutrino transport scheme with elaborate neutrino opacities.

In order to clarify whether we can or cannot detect the SASI-induced modulation in the GW and neutrino signals, we primarily need to perform a GW signal reconstruction study (e.g., Hayama et al. 2015; Gossan et al. 2016; Powell et al. 2016) using nonstationary and non-Gaussian noise (Powell et al. 2016, 2017). This is the most urgent task that we have to investigate as a sequel of this work. For a Galactic event, we need third-generation detectors for observing the SASI-modulated GW signals (e.g., Andresen et al. 2017), whereas the neutrino signals could be surely detected by IceCube and Super-K (Tamborra et al. 2013). The neutrino burst can be used to determine the core bounce time (Halzen & Raffelt 2009), which significantly raises the detection efficiency of the GWs (e.g., Gossan et al. 2016; Nakamura et al. 2016). Our current study extends the horizon of previous prediction, such as when we would succeed the simultaneous detection of neutrino and GW signals from future nearby CCSN event, we could infer the supernova triggering dynamics (e.g., the SASI) from the following specific features: (1) the low-frequency ($F \sim 100$ Hz) modulation in both GW and neutrino signal and (2) a few 10 ms time delay of the SASI-modulated GW signal from the SASI-modulated neutrino event rate. We finally note that the nondetection of the correlation could be hypothetically used as a measure to constrain the nuclear EOSs. From the limited number of the EOSs used in this work, one cannot obtain any quantitative conclusions. Recently, a number of nuclear EOS became available (see Oertel et al. 2017 for a review). Using such a rich variety of the EOSs, one could in principle do this, but only if one could afford enough computational time to make the many 3D CCSN runs doable.

T.K. was supported by the European Research Council (ERC; FP7) under ERC Advanced Grant Agreement N° 321263—FISH and ERC StG EUROPIUM-677912. Numerical computations were carried out on Cray XC30 at Center for Computational Astrophysics, National Astronomical Observatory of Japan. K.K. was thankful for stimulating discussions with E. Müller, H. T. Janka, and T. Foglizzo. This study was supported by JSPS KAKENHI Grant Nos. JP15H00789, JP15H01039, JP15KK0173, JP17H01130, JP17H05206, JP17K14306, and JP17H06364 and JICFuS as a priority issue to be tackled by using Post "K" Computer.

ORCID iDs

Takami Kuroda https://orcid.org/0000-0001-5168-6792
Kei Kotake https://orcid.org/0000-0003-2456-6183

References

Abbasi, R., Abdou, Y., Abu-Zayyad, T., et al. 2011a, A&A, 535, A109
Abbasi, R., Abdou, Y., Abu-Zayyad, T., et al. 2011b, A&A, 535, A109
Abbott, B. P., Abbott, R., Abbott, T. D., et al. 2016, PhRvL, 116, 061102
Abbott, B. P., Abbott, R., Abbott, T. D., et al. 2017, CQGra, 34, 044001
Abe, K. 2016, Hyper Kamiokande Public Design Report, KEK-PREPRINT-2016-21, http://www.hyperk.org/?p=215
Andresen, H., Müller, B., Müller, E., & Janka, H.-T. 2017, MNRAS, 468, 2032
Antoniadis, J., Freire, P. C. C., Wex, N., et al. 2013, Sci, 340, 448
Aso, Y., Michimura, Y., Somiya, K., et al. 2013, PhRvD, 88, 043007
Baumgarte, T. W., & Shapiro, S. L. 1999, PhRvD, 59, 024007
Bethe, H. A. 1990, RvMP, 62, 801
Bionta, R. M., Blewitt, G., Bratton, C. B., Casper, D., & Ciocio, A. 1987, PhRvL, 58, 1494
Blondin, J. M., Mezzacappa, A., & DeMarino, C. 2003, ApJ, 584, 971
Bollig, R., Janka, H.-T., Lohs, A., et al. 2017, arXiv:1706.04630
Brandt, T. D., Burrows, A., Ott, C. D., & Livne, E. 2011, ApJ, 728, 8
Buras, R., Rampp, M., Janka, H.-T., & Kifonidis, K. 2006, A&A, 447, 1049
Burrows, A. 2013, RvMP, 85, 245
Burrows, A., Vartanyan, D., Dolence, J. C., Skinner, M. A., & Radice, D. 2016, arXiv:1611.05859
Cerdá-Durán, P., DeBrye, N., Aloy, M. A., Font, J. A., & Obergaulinger, M. 2013, ApJL, 779, L18
Chakraborty, S., Hansen, R., Izaguirre, I., & Raffelt, G. 2016, NuPhB, 908, 366
Couch, S. M. 2013, ApJ, 775, 35
Demorest, P. B., Pennucci, T., Ransom, S. M., Roberts, M. S. E., & Hessels, J. W. T. 2010, Natur, 467, 1081
Duan, H., Fuller, G. M., & Qian, Y.-Z. 2010, ARNPS, 60, 569
Fernández, R. 2015, MNRAS, 452, 2071
Fischer, T. 2016, A&A, 593, A103
Fischer, T., Hempel, M., Sagert, I., Suwa, Y., & Schaffner-Bielich, J. 2014, EPJA, 50, 46
Foglizzo, T. 2002, A&A, 392, 353
Foglizzo, T., Kazeroni, R., Guilet, J., et al. 2015, PASA, 32, e009
Foglizzo, T., Scheck, L., & Janka, H.-T. 2006, ApJ, 652, 1436
Fryer, C. L., & New, K. C. B. 2011, LRR, 14, 1
Gossan, S. E., Sutton, P., Stuver, A., et al. 2016, PhRvD, 93, 042002
Grefenstette, B. W., Fryer, C. L., Harrison, F. A., et al. 2017, ApJ, 834, 19
Halzen, F., & Raffelt, G. G. 2009, PhRvD, 80, 087301
Hanke, F., Marek, A., Müller, B., & Janka, H.-T. 2012, ApJ, 755, 138
Hanke, F., Müller, B., Wongwathanarat, A., Marek, A., & Janka, H.-T. 2013, ApJ, 770, 66
Harry, G. M. & LIGO Scientific Collaboration 2010, CQGra, 27, 084006
Hayama, K., Kuroda, T., Kotake, K., & Takiwaki, T. 2015, PhRvD, 92, 122001
Heger, A., Woosley, S. E., & Spruit, H. C. 2005, ApJ, 626, 350
Hempel, M., & Schaffner-Bielich, J. 2010, NuPhA, 837, 210
Hild, S., Freise, A., Mantovani, M., et al. 2009, CQGra, 26, 025005
Hirata, K., Kajita, T., Koshiba, M., Nakahata, M., & Oyama, Y. 1987, PhRvL, 58, 1490
Holland-Ashford, T., Lopez, L. A., Auchettl, K., Temim, T., & Ramirez-Ruiz, E. 2017, ApJ, 844, 84
Horowitz, C. J., Caballero, O. L., Lin, Z., O'Connor, E., & Schwenk, A. 2017, PhRvC, 95, 025801
Ikeda, M., Takeda, A., Fukuda, Y., et al. 2007, ApJ, 669, 519
Janka, H.-T. 2017, arXiv:1702.08825
Kotake, K. 2013, CRPhy, 14, 318
Kotake, K., Iwakami, W., Ohnishi, N., & Yamada, S. 2009, ApJL, 697 L133
Kotake, K., & Kuroda, T. 2016, in Gravitational Waves from Core-Collapse Supernovae, ed. P. M. Athem & W. Alsabti (Berlin: Springer), 27
Kotake, K., Takiwaki, T., Suwa, Y., et al. 2012, AdAst, 2012 arXiv:1204.2330
Kuroda, T., Kotake, K., & Takiwaki, T. 2012, ApJ, 755, 11
Kuroda, T., Kotake, K., & Takiwaki, T. 2016a, ApJL, 829, L14
Kuroda, T., Takiwaki, T., & Kotake, K. 2014, PhRvD, 89, 044011
Kuroda, T., Takiwaki, T., & Kotake, K. 2016b, ApJS, 222, 20
Larsson, J., Fransson, C., Spyromilio, J., et al. 2016, ApJ, 833, 147
Lattimer, J. M., & Lim, Y. 2013, ApJ, 771, 51
Lentz, E. J., Mezzacappa, A., Bronson Messer, O. E., Hix, W. R., & Bruenn, S. W. 2012, ApJ, 760, 94
Lund, T., Marek, A., Lunardini, C., Janka, H.-T., & Raffelt, G. 2010, PhRvD, 82, 063007
Marek, A., & Janka, H.-T. 2009, ApJ, 694, 664
Marek, A., Janka, H.-T., & Müller, E. 2009, A&A, 496, 475
Martínez-Pinedo, G., Fischer, T., Lohs, A., & Huther, L. 2012, PhRvL, 109, 251104
Melson, T., Janka, H.-T., Bollig, R., et al. 2015, ApJL, 808, L42
Mikheyev, S. P., & Smirnov, A. Y. 1985, YaFiz, 42, 1441
Mirizzi, A., Tamborra, I., Janka, H.-T., et al. 2016, NCimR, 39, 1
Misner, C. W., Thorne, K. S., & Wheeler, J. A. 1973, Gravitation (San Francisco: Freeman)

Mösta, P., Richers, S., Ott, C. D., et al. 2014, ApJL, 785, L29
Müller, B. 2016, PASA, 33, e048
Müller, B., & Janka, H.-T. 2014, ApJ, 788, 82
Müller, B., Janka, H.-T., & Marek, A. 2013, ApJ, 766, 43
Müller, E., & Janka, H.-T. 1997, A&A, 317, 140
Müller, E., Rampp, M., Buras, R., Janka, H.-T., & Shoemaker, D. H. 2004, ApJ, 603, 221
Murphy, J. W., Dolence, J. C., & Burrows, A. 2013, ApJ, 771, 52
Murphy, J. W., Ott, C. D., & Burrows, A. 2009, ApJ, 707, 1173
Nakamura, K., Horiuchi, S., Tanaka, M., et al. 2016, MNRAS, 461, 3296
Nakamura, K., Takiwaki, T., Kuroda, T., & Kotake, K. 2015, PASJ, 67, 107
Obergaulinger, M., & Aloy, M. Á 2017, MNRAS, 469, L43
O'Connor, E., & Ott, C. D. 2011, ApJ, 730, 70
Oertel, M., Hempel, M., Klähn, T., & Typel, S. 2017, RvMP, 89, 015007
Ott, C. D. 2009, CQGra, 26, 063001
Ott, C. D., Abdikamalov, E., O'Connor, E., et al. 2012, PhRvD, 86, 024026
Powell, J., Gossan, S. E., Logue, J., & Heng, I. S. 2016, PhRvD, 94, 123012
Powell, J., Szczepanczyk, M., & Heng, I. S. 2017, arXiv:1709.00955
Punturo, M , Lück, H., & Beker, M. 2014, in Advanced Interferometers and the Search for Gravitational Waves, ed. M. Bassan (Dordrecht: Springer), 333
Roberts, L. F., Ott, C. D., Haas, R., et al. 2016, ApJ, 831, 98
Roberts, L. F., & Reddy, S. 2017, PhRvC, 95, 045807
Sathyaprakash, B. S., & Schutz, B. F. 2009, LRR, 12, 2
Scheck, L., Janka, H.-T., Foglizzo, T., & Kifonidis, K. 2008, A&A, 477, 931
Scheidegger, S., Käppeli, R., Whitehouse, S. C., Fischer, T., & Liebendörfer, M. 2010, A&A, 514, A51
Scholberg, K. 2012, ARNPS, 62, 81
Shibata, M., & Nakamura, T. 1995, PhRvD, 52, 5428
Steiner, A. W., Hempel, M., & Fischer, T. 2013, ApJ, 774, 17
Takiwaki, T., Kotake, K., & Suwa, Y. 2016, MNRAS, 461, L112
Tamborra, I., Hanke, F., Janka, H.-T., et al. 2014a, ApJ, 792, 96
Tamborra, I., Hanke, F., Müller, B., Janka, H.-T., & Raffelt, G. 2013, PhRvL, 111, 121104
Tamborra, I., Raffelt, G., Hanke, F., Janka, H.-T., & Müller, B. 2014b, PhRvD, 90, 045032
Tanaka, M., Maeda, K., Mazzali, P. A., Kawabata, K. S., & Nomoto, K. 2017, ApJ, 837, 105
Wolfenstein, L. 1978, PhRvD, 17, 2369
Woosley, S. E., Heger, A., & Weaver, T. A. 2002, RvMP, 74, 1015
Woosley, S. E., & Weaver, T. A. 1995, ApJS, 101, 181
Yakunin, K. N., Mezzacappa, A., Marronetti, P., et al. 2015, PhRvD, 92, 084040
Yakunin, K. N., Mezzacappa, A., Marronetti, P., et al. 2017, arXiv:1701.07325
Yokozawa, T., Asano, M., Kayano, T., et al. 2015, ApJ, 811, 86